Editors' Suggestion | Featured in Physics

Properties of Cosmic Deuterons Measured by the Alpha Magnetic Spectrometer

M. Aguilar,[29] B. Alpat,[35] G. Ambrosi,[35] H. Anderson,[10] L. Arruda,[27] N. Attig,[24] C. Bagwell,[10] F. Barao,[27] M. Barbanera,[35] L. Barrin,[14] A. Bartoloni,[39] R. Battiston,[46,47] A. Bayyari,[20] N. Belyaev,[10] B. Bertucci,[35,36] V. Bindi,[20] K. Bollweg,[21] J. Bolster,[10] M. Borchiellini,[17] B. Borgia,[39,40] M. J. Boschini,[31] M. Bourquin,[15] C. Brugnoni,[35,36] J. Burger,[10] W. J. Burger,[46] X. D. Cai,[10] M. Capell,[10] J. Casaus,[29] G. Castellini,[13] F. Cervelli,[37] Y. H. Chang,[44] G. M. Chen,[6,7] G. R. Chen,[23] H. Chen,[19] H. S. Chen,[6,7] Y. Chen,[23] L. Cheng,[23] H. Y. Chou,[44] S. Chouridou,[1] V. Choutko,[10] C. H. Chung,[1] C. Clark,[10,21] G. Coignet,[3] C. Consolandi,[20] A. Contin,[8,9] C. Corti,[20] Z. Cui,[22,23] K. Dadzie,[10] F. D'Angelo,[9,8] A. Dass,[46,47] C. Delgado,[29] S. Della Torre,[31] M. B. Demirköz,[2] L. Derome,[16] S. Di Falco,[37] V. Di Felice,[41] C. Díaz,[29] F. Dimiccoli,[46] P. von Doetinchem,[20] F. Dong,[33] F. Donnini,[35] M. Duranti,[35] A. Egorov,[10] A. Eline,[10] F. Faldi,[35,36] D. Fehr,[1] J. Feng,[18] E. Fiandrini,[35,36] P. Fisher,[10] V. Formato,[41] C. Gámez,[29] R. J. García-López,[26] C. Gargiulo,[14] H. Gast,[1] M. Gervasi,[31,32] F. Giovacchini,[29] D. M. Gómez-Coral,[30] J. Gong,[33] D. Grandi,[31,32] M. Graziani,[35,36] A. N. Guracho,[39] S. Haino,[44] K. C. Han,[28] R. K. Hashmani,[2] Z. H. He,[18] B. Heber,[25] T. H. Hsieh,[10] J. Y. Hu,[6,7] B. W. Huang,[19] M. Ionica,[35] M. Incagli,[37] Yi Jia,[10] H. Jinchi,[28] G. Karagöz,[2] S. Khan,[15] B. Khiali,[41] Th. Kirn,[1] A. P. Klipfel,[10] O. Kounina,[10] A. Kounine,[10] V. Koutsenko,[10] D. Krasnopevtsev,[10] A. Kuhlman,[20] A. Kulemzin,[10] G. La Vacca,[31,32] E. Laudi,[14] G. Laurenti,[8] G. LaVecchia,[10] I. Lazzizzera,[46,47] H. T. Lee,[43] S. C. Lee,[44] H. L. Li,[23] J. Q. Li,[33] M. Li,[15] M. Li,[22] Q. Li,[33] Q. Li,[22] Q. Y. Li,[23] S. Li,[1] S. L. Li,[6,7] J. H. Li,[22] Z. H. Li,[6,7] M. J. Liang,[6,7] P. Liao,[22] C. H. Lin,[44] T. Lippert,[24] J. H. Liu,[5] P. C. Liu,[23] S. Q. Lu,[44] Y. S. Lu,[6] K. Luebelsmeyer,[1,*] J. Z. Luo,[33] Q. Luo,[18] S. D. Luo,[19] Xi Luo,[23] C. Mañá,[29] J. Marín,[29] J. Marquardt,[25] G. Martínez,[29] N. Masi,[8] D. Maurin,[16] T. Medvedeva,[10] A. Menchaca-Rocha,[30] Q. Meng,[33] V. V. Mikhailov,[23] M. Molero,[26] P. Mott,[10,21] L. Mussolin,[35,36] Y. Najafi Jozani,[1] R. Nicolaidis,[47,46] N. Nikonov,[20] F. Nozzoli,[46] J. Ocampo-Peleteiro,[29] A. Oliva,[8] M. Orcinha,[35,36] F. Palmonari,[8,9] M. Paniccia,[15] A. Pashnin,[10] M. Pauluzzi,[35,36] S. Pensotti,[31,32] P. Pietzcker,[25] V. Plyaskin,[10] S. Poluianov,[34] D. Pridöhl,[1] Z. Y. Qu,[23] L. Quadrani,[8,9] P. G. Rancoita,[31] D. Rapin,[15] A. Reina Conde,[8] E. Robyn,[15] I. Rodríguez-García,[29] L. Romaneehsen,[25] F. Rossi,[47,46] A. Rozhkov,[10] D. Rozza,[31] R. Sagdeev,[11] E. Savin,[9,8] S. Schael,[1] A. Schultz von Dratzig,[1] G. Schwering,[1] E. S. Seo,[12] B. S. Shan,[4] A. Shukla,[20] T. Siedenburg,[1] G. Silvestre,[35] J. W. Song,[22] X. J. Song,[23] R. Sonnabend,[1] L. Strigari,[39,†] T. Su,[23] Q. Sun,[22] Z. T. Sun,[6,7] L. Tabarroni,[41] M. Tacconi,[31,32] Z. C. Tang,[6] J. Tian,[41] Y. Tian,[19] Samuel C. C. Ting,[10,14] S. M. Ting,[10] N. Tomassetti,[35,36] J. Torsti,[48] T. Urban,[10,21] I. Usoskin,[34] V. Vagelli,[38,35] R. Vainio,[48] M. Valencia-Otero,[45] E. Valente,[39,40] E. Valtonen,[48] M. Vázquez Acosta,[26] M. Vecchi,[17] M. Velasco,[29] C. X. Wang,[22] L. Wang,[5] L. Q. Wang,[22] N. H. Wang,[22] Q. L. Wang,[5] S. Wang,[20] X. Wang,[10] Z. M. Wang,[23] J. Wei,[15,23] Z. L. Weng,[10] H. Wu,[33] Y. Wu,[23] Z. B. Wu,[22] J. N. Xiao,[19] R. Q. Xiong,[33] X. Z. Xiong,[19] W. Xu,[22,23] Q. Yan,[10] H. T. Yang,[6,7] Y. Yang,[42] A. Yelland,[10] H. Yi,[33] Y. H. You,[6,7] Y. M. Yu,[10] Z. Q. Yu,[6] C. Zhang,[6] F. Z. Zhang,[6,7] J. Zhang,[22] J. H. Zhang,[33] Z. Zhang,[10] P. W. Zhao,[18] C. Zheng,[23] Z. M. Zheng,[4] H. L. Zhuang,[6] V. Zhukov,[1] A. Zichichi,[8,9] and P. Zuccon[46,47]

(AMS Collaboration)

[1]*I. Physics Institute and JARA-FAME, RWTH Aachen University, 52056 Aachen, Germany*
[2]*Department of Physics, Middle East Technical University (METU), 06800 Ankara, Türkiye*
[3]*Université Grenoble Alpes, Université Savoie Mont Blanc, CNRS, LAPP-IN2P3, 74000 Annecy, France*
[4]*Beihang University (BUAA), Beijing 100191, China*
[5]*Institute of Electrical Engineering (IEE), Chinese Academy of Sciences, Beijing 100190, China*
[6]*Institute of High Energy Physics (IHEP), Chinese Academy of Sciences, Beijing 100049, China*
[7]*University of Chinese Academy of Sciences (UCAS), Beijing 100049, China*
[8]*INFN Sezione di Bologna, 40126 Bologna, Italy*
[9]*Università di Bologna, 40126 Bologna, Italy*
[10]*Massachusetts Institute of Technology (MIT), Cambridge, Massachusetts 02139, USA*
[11]*East-West Center for Space Science, University of Maryland, College Park, Maryland 20742, USA*
[12]*IPST, University of Maryland, College Park, Maryland 20742, USA*
[13]*CNR–IROE, 50125 Firenze, Italy*
[14]*European Organization for Nuclear Research (CERN), 1211 Geneva 23, Switzerland*
[15]*DPNC, Université de Genève, 1211 Genève 4, Switzerland*
[16]*Université Grenoble Alpes, CNRS, Grenoble INP, LPSC-IN2P3, 38000 Grenoble, France*
[17]*Kapteyn Astronomical Institute, University of Groningen, P.O. Box 800, 9700 AV Groningen, Netherlands*

[18]Sun Yat–Sen University (SYSU), Guangzhou 510275, China
[19]Zhejiang University (ZJU), Hangzhou 310058, China
[20]Physics and Astronomy Department, University of Hawaii, Honolulu, Hawaii 96822, USA
[21]National Aeronautics and Space Administration Johnson Space Center (JSC), Houston, Texas 77058, USA
[22]Shandong University (SDU), Jinan, Shandong 250100, China
[23]Shandong Institute of Advanced Technology (SDIAT), Jinan, Shandong 250100, China
[24]Jülich Supercomputing Centre and JARA-FAME, Research Centre Jülich, 52425 Jülich, Germany
[25]Institut für Experimentelle und Angewandte Physik, Christian-Albrechts-Universität zu Kiel, 24118 Kiel, Germany
[26]Instituto de Astrofísica de Canarias (IAC), 38205 La Laguna, Spain and Departamento de Astrofísica, Universidad de La Laguna, 38206 La Laguna, Tenerife, Spain
[27]Laboratório de Instrumentação e Física Experimental de Partículas (LIP), 1649-003 Lisboa, Portugal
[28]National Chung-Shan Institute of Science and Technology (NCSIST), Longtan, Tao Yuan 32546, Taiwan
[29]Centro de Investigaciones Energéticas, Medioambientales y Tecnológicas (CIEMAT), 28040 Madrid, Spain
[30]Instituto de Física, Universidad Nacional Autónoma de México (UNAM), Ciudad de México 01000, Mexico
[31]INFN Sezione di Milano–Bicocca, 20126 Milano, Italy
[32]Università di Milano–Bicocca, 20126 Milano, Italy
[33]Southeast University (SEU), Nanjing 210096, China
[34]Sodankylä Geophysical Observatory and Space Physics and Astronomy Research Unit, University of Oulu, 90014 Oulu, Finland
[35]INFN Sezione di Perugia, 06100 Perugia, Italy
[36]Università di Perugia, 06100 Perugia, Italy
[37]INFN Sezione di Pisa, 56100 Pisa, Italy
[38]Agenzia Spaziale Italiana (ASI), 00133 Roma, Italy
[39]INFN Sezione di Roma 1, 00185 Roma, Italy
[40]Università di Roma La Sapienza, 00185 Roma, Italy
[41]INFN Sezione di Roma Tor Vergata, 00133 Roma, Italy
[42]National Cheng Kung University, Tainan 70101, Taiwan
[43]Academia Sinica Grid Center (ASGC), Nankang, Taipei, 11529, Taiwan
[44]Institute of Physics, Academia Sinica, Nankang, Taipei 11529, Taiwan
[45]Physics Department and Center for High Energy and High Field Physics, National Central University (NCU), Tao Yuan 32054, Taiwan
[46]INFN TIFPA, 38123 Trento, Italy
[47]Università di Trento, 38123 Trento, Italy
[48]Space Research Laboratory, Department of Physics and Astronomy, University of Turku, 20014 Turku, Finland

(Received 5 February 2024; revised 22 March 2024; accepted 6 May 2024; published 25 June 2024)

Precision measurements by the Alpha Magnetic Spectrometer (AMS) on the International Space Station of the deuteron (D) flux are presented. The measurements are based on 21×10^6 D nuclei in the rigidity range from 1.9 to 21 GV collected from May 2011 to April 2021. We observe that over the entire rigidity range the D flux exhibits nearly identical time variations with the p, ^{3}He, and ^{4}He fluxes. Above 4.5 GV, the $D/^4$He flux ratio is time independent and its rigidity dependence is well described by a single power law $\propto R^{\Delta}$ with $\Delta_{D/^4\mathrm{He}} = -0.108 \pm 0.005$. This is in contrast with the ^{3}He/^{4}He flux ratio for which we find $\Delta_{^3\mathrm{He}/^4\mathrm{He}} = -0.289 \pm 0.003$. Above ~13 GV we find a nearly identical rigidity dependence of the D and p fluxes with a D/p flux ratio of 0.027 ± 0.001. These unexpected observations indicate that cosmic deuterons have a sizable primarylike component. With a method independent of cosmic ray propagation, we obtain the primary component of the D flux equal to $9.4 \pm 0.5\%$ of the ^{4}He flux and the secondary component of the D flux equal to $58 \pm 5\%$ of the ^{3}He flux.

DOI: 10.1103/PhysRevLett.132.261001

Introduction.—Hydrogen nuclei are the most abundant cosmic ray species. They consist of two stable isotopes, protons (p) and deuterons (D). Big Bang nucleosynthesis predicts a very small production of deuterium and, with time, the abundance of D decreases from its primordial value, with the measured D/p ratio in the interstellar medium of $\sim 2 \times 10^{-5}$ [1]. Instead of being accelerated in supernova

remnants like primary cosmic rays p and ^{4}He, deuterons are thought to overwhelmingly originate from interactions of He with the interstellar medium. Together with ^{3}He, deuterons are called secondary cosmic rays [2,3]. Earlier, we have found that heavier secondary cosmic rays Li, Be, and B have the same rigidity dependence as each other [4].

Deuteron and He interaction cross sections with the interstellar medium are significantly smaller than those of heavier nuclei [5]. Explicitly, the $D/^4$He and ^{3}He/^{4}He flux ratios probe the properties of diffusion at larger distances than those probed by heavier nuclei, and, therefore, provide unique input to cosmic ray propagation models [6–11].

Previously, the ^{3}He and ^{4}He fluxes have been published by AMS with a typical error of ∼2% [12]. There have been measurements of deuteron and helium isotope fluxes and their ratios as functions of kinetic energy per nucleon with large (∼40%) errors [13–17]. There are no previous measurements of the $D/^4$He flux ratio as a function of rigidity.

In this Letter, precision measurements of the D flux are presented in the rigidity range from 1.9 to 21 GV, based on 21×10^6 D nuclei collected by AMS. The D flux error at 10 GV is 3.0%.

Detector.—The AMS detector layout and description are presented in Refs. [18,19] and shown in Fig. S1 of the Supplemental Material [20]. The elements used in this analysis are the magnet [21], the silicon tracker [22–25], the time of flight counters (TOF) [26], and the ring imaging Čerenkov detector (RICH) [27]. Further information on the AMS layout, performance, trigger, and the Monte Carlo simulations (MC) [28–30] is presented in the Supplemental Material [20].

Selection.—AMS has collected 1.8×10^{11} cosmic ray events. D events are required to be downward going and to have a reconstructed track in the inner tracker which passes through $L1$, the top layer of the silicon tracker. Charge measurements on $L1$, the upper TOF, the inner tracker, and the lower TOF are required to be compatible with charge number $Z = 1$. Details of the event selection are provided in the Supplemental Material [20]. Background to D comes overwhelmingly from He fragmentation $\mathrm{He} \to D$ in the AMS materials, mostly C and Al, above $L1$. This background has been computed from data using the reaction $^4\mathrm{He} + (\mathrm{C}, \mathrm{Al}) \to T + X$, where T are tritium nuclei, see Fig. S2 and discussion in Ref. [12] and in the Supplemental Material [20], and it has been found to be ≤4% over the entire rigidity range.

Analysis.—The flux of deuterons is measured in 26 rigidity bins ranging from 1.9 to 21 GV chosen according to Ref. [12]. To compute the deuteron contribution in the overall $Z = 1$ flux, an unfolding procedure, similar to Ref. [12] with the methods of Ref. [31] has been applied, as detailed in the Supplemental Material [20].

The isotropic flux Φ_i in the ith rigidity bin $(R_i, R_i + \Delta R_i)$ is given by

$$\Phi_i = \frac{N_i}{A_i \epsilon_i \Delta R_i T_i}, \tag{1}$$

where N_i is the background subtracted number of events in rigidity bin i, A_i the effective acceptance, ϵ_i the trigger efficiency, ΔR_i the bin width, and T_i is the collection time.

Extensive studies were made on the systematic errors. The systematic errors in N_i are due to uncertainties in the rigidity and velocity resolution functions, unfolding procedure, and background subtraction. The rigidity resolution function, determined from MC simulations, has been extensively verified with the data [32]. The inverse velocity $(1/\beta)$ resolution functions of the TOF and the RICH were first studied at $\beta \simeq 1$ with data, as shown in Fig. S4 of the Supplemental Material [20]. The dependence of the velocity resolution functions on β was obtained from MC simulations and corrected with data, resulting in corrections of <5% both for the TOF and the RICH. The systematic uncertainty of N_i due to the uncertainties in rigidity and velocity resolution functions and unfolding procedure has been evaluated to be 3.2% at 2 GV, decreasing to 1% at 10 GV and remaining at this value up to 21 GV. The systematic uncertainty of N_i from the background subtraction is <1% over the entire rigidity range.

Other sources of systematic error include uncertainties in the trigger efficiency, in the geomagnetic cutoff, and in the effective acceptance. The trigger efficiency has been measured as described in Ref. [32]. The systematic error on the fluxes due to the trigger efficiency uncertainties is <1% over the entire rigidity range. The geomagnetic cutoff factor was varied from 1.0 to 1.4, resulting in a negligible systematic uncertainty <0.1% in the entire rigidity range.

The effective acceptances A_i were calculated from the MC simulation and then corrected for differences between the data and simulated events related to (a) event reconstruction and selection, namely, in the efficiencies of track finding, charge determination, tracker quality cuts, and velocity quality cuts, and (b) inelastic interactions of D in the AMS materials. The total correction to the effective acceptances was found to be <10% over the entire rigidity range. The systematic error on the D flux associated to (a) has been found to be <1% below 3 GV, 2.5% between 3 and 8 GV, and <1% above 8 GV. The systematic error associated to (b) on the D flux was found to be <2.5% over the entire rigidity range.

The variations of the trigger and reconstruction efficiencies were studied as a function of time. A time-dependent systematic error due to the variations of trigger and reconstruction efficiencies for different time periods was estimated to be <1% in the entire rigidity range. All the other systematic errors are time independent.

Most importantly, independent analyses were performed on the same data sample by four independent study groups. The results of these analyses are consistent with this Letter.

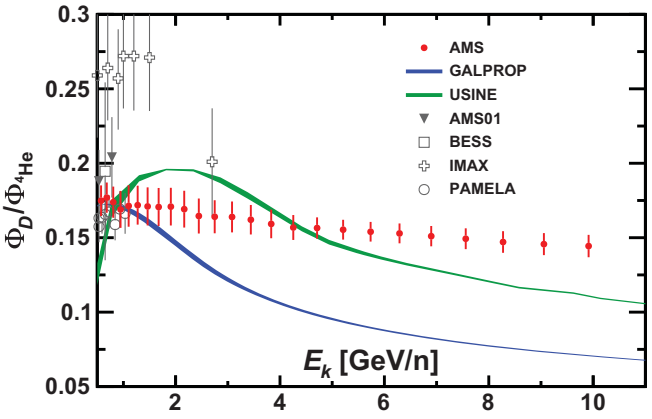

FIG. 1. The AMS $D/^4$He flux ratio as a function of kinetic energy per nucleon with total errors, together with previous measurements [14–17] and the predictions of the recent propagation models GALPROP [34] (blue shaded area) and USINE [35] (green shaded area). The shaded areas show the variations of the model predictions due to solar modulation. As seen, the AMS results on the $D/^4$He flux ratio disagree with the GALPROP predictions above $\sim$2 GeV/n and disagree with the USINE predictions from $\sim$1.5 to 3.5 GeV/n and above $\sim$5 GeV/n.

Results.—The D fluxes are measured as functions of the rigidity from May 2011 to April 2021 in 33 time periods of four Bartels rotations (108 days) each. To compare the time and rigidity dependence of the D fluxes with the ^{3}He and ^{4}He fluxes, the ^{3}He and ^{4}He flux measurements of Ref. [12] were extended to April 2021 and to the rigidity range from 1.9 to 21 GV. The resulting ^{3}He and ^{4}He fluxes are consistent with Ref. [12] over the overlapping time period and rigidity range. The D, ^{3}He, and ^{4}He fluxes and the flux ratios are presented in Tables S1–S99 in the Supplemental Material [20,33], including statistical and systematic errors. For the fluxes, the contributions of individual independent sources to the systematic error were added in quadrature to obtain the total systematic uncertainty. For the D and ^{3}He/^{4}He flux ratios the correlation of the systematic errors is taken into account to evaluate the total systematic error.

Figure 1 shows the AMS time-averaged $D/^4$He flux ratio as a function of kinetic energy per nucleon together with earlier measurements [14–17] and predictions from the recent cosmic ray propagation models, GALPROP [34] and USINE [35]. Figure S6 of the Supplemental Material [20] shows the AMS time-averaged D/He flux ratio as a function of kinetic energy per nucleon together with earlier measurements [13–16] and predictions from the GALPROP and USINE propagation models. Data from other experiments have been extracted using Ref. [36]. As seen, the AMS results on the $D/^4$He and on the D/He flux ratios disagree with the GALPROP predictions above $\sim$2 GeV/n and disagree with the USINE predictions from $\sim$1.5 to 3.5 GeV/n and above $\sim$5 GeV/n. Future models may provide alternative interpretations of our data.

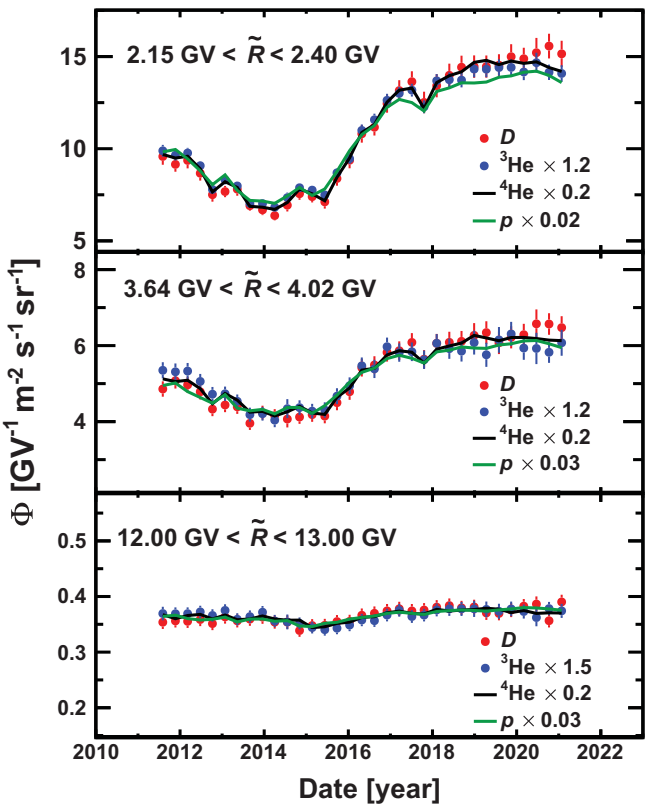

FIG. 2. The AMS D (red points), ^{3}He (blue points), ^{4}He (black curves), and p (green curves) fluxes as functions of time for three characteristic rigidity bins. The ^{3}He, ^{4}He, and p fluxes have been scaled to obtain the same time-averaged flux as D in each rigidity bin. The errors are the quadratic sum of the statistical and time-dependent systematic errors. As seen, in each rigidity bin the four fluxes show a similar time behavior.

Figure 2 shows the AMS D flux as a function of time for three characteristic rigidity bins, compared with the AMS p, ^{3}He, and ^{4}He fluxes. The p fluxes were extracted from Ref. [37], with the D fluxes subtracted. As seen, all spectra exhibit nearly identical variations with time and the relative magnitude of the variations decreases with increasing rigidity.

To study the differences in time variation for the D, ^{3}He, and ^{4}He fluxes in detail we fit a linear relation between the relative variations of $\Phi_D/\Phi_{^4\mathrm{He}}$ and $\Phi_{^3\mathrm{He}}/\Phi_{^4\mathrm{He}}$ and of $\Phi_{^4\mathrm{He}}$ for the ith rigidity bin, $(R_i, R_i + \Delta R_i)$, as

$$\frac{\Phi^i_D/\Phi^i_{^4\mathrm{He}} - \langle \Phi^i_D/\Phi^i_{^4\mathrm{He}} \rangle}{\langle \Phi^i_D/\Phi^i_{^4\mathrm{He}} \rangle} = k^i_D \frac{\Phi^i_{^4\mathrm{He}} - \langle \Phi^i_{^4\mathrm{He}} \rangle}{\langle \Phi^i_{^4\mathrm{He}} \rangle}, \quad (2)$$

$$\frac{\Phi^i_{^3\mathrm{He}}/\Phi^i_{^4\mathrm{He}} - \langle \Phi^i_{^3\mathrm{He}}/\Phi^i_{^4\mathrm{He}} \rangle}{\langle \Phi^i_{^3\mathrm{He}}/\Phi^i_{^4\mathrm{He}} \rangle} = k^i_{^3\mathrm{He}} \frac{\Phi^i_{^4\mathrm{He}} - \langle \Phi^i_{^4\mathrm{He}} \rangle}{\langle \Phi^i_{^4\mathrm{He}} \rangle}, \quad (3)$$

where k^i_D and $k^i_{^3\mathrm{He}}$ are the slopes of the $\Phi^i_D/\Phi^i_{^4\mathrm{He}}$ and $\Phi^i_{^3\mathrm{He}}/\Phi^i_{^4\mathrm{He}}$ linear dependence, and $\langle \Phi^i_D/\Phi^i_{^4\mathrm{He}} \rangle$, $\langle \Phi^i_{^3\mathrm{He}}/\Phi^i_{^4\mathrm{He}} \rangle$

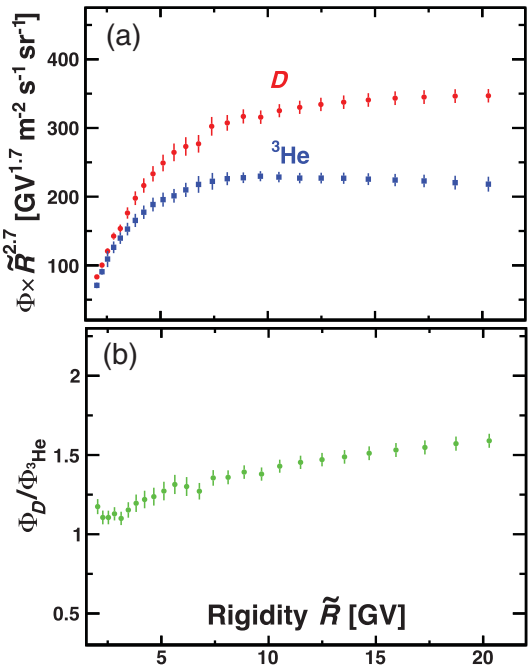

FIG. 3. (a) The AMS time-averaged D (red) and ^{3}He (blue) fluxes multiplied by $\tilde{R}^{2.7}$ as functions of rigidity with total errors. (b) The AMS time-averaged $D/^3$He flux ratio as a function of rigidity with total errors.

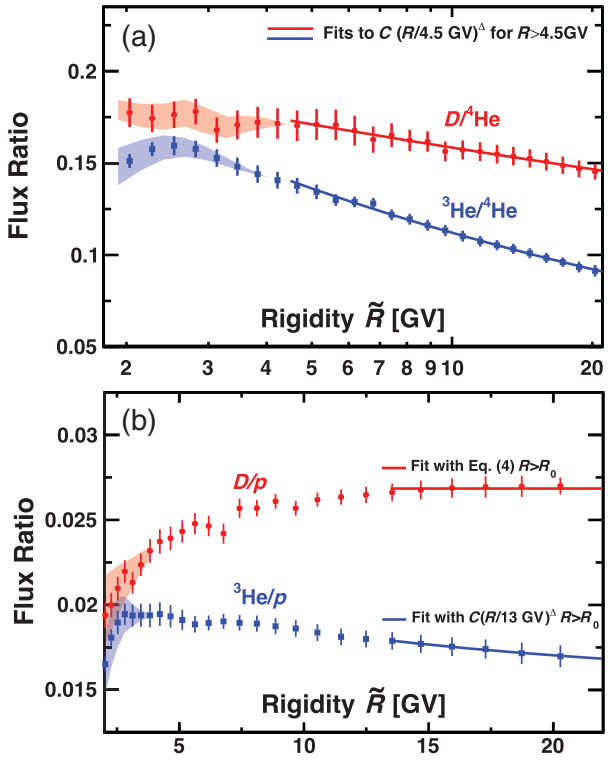

FIG. 4. (a) The AMS time-averaged D (red circles) and ^{3}He/^{4}He (blue squares) flux ratios as functions of rigidity with total errors. Red and blue curves show power law fits $C(R/4.5\ \mathrm{GV})^{\Delta}$ for $R > 4.5$ GV to the D and ^{3}He/^{4}He flux ratios respectively. (b) The AMS D/p and ^{3}He/p flux ratios as functions of rigidity with total errors. The solid red curve shows the D/p flux ratio fit result with Eq. (4). For display purposes only, the fit results are only shown for $R > R_0$. The solid blue curve shows the ^{3}He/p flux ratio fit with $C(R/13\ \mathrm{GV})^{\Delta}$ above R_0. As seen, the D/p flux ratio increases with rigidity and becomes a constant above $R_0 \sim 13$ GV, while the ^{3}He/p flux ratio decreases with rigidity. Shaded areas show corresponding flux ratio time variations at low rigidities.

are the $D/^4$He, ^{3}He/^{4}He flux ratio averages, and $\langle \Phi^i_{^4\mathrm{He}} \rangle$ is the ^{4}He flux average. The averages are taken over the entire data taking period. Figure S7 of the Supplemental Material [20] shows the AMS $D/^4$He (left panels) and ^{3}He/^{4}He (right panels) flux ratios as functions of the ^{4}He flux for three characteristic rigidity bins, together with the slopes k obtained with Eqs. (2) and (3), respectively. Figure S8 of the Supplemental Material [20] shows the fit results of the slopes k as functions of rigidity from 1.9 to 7.8 GV. As seen, k_D is significantly above zero for rigidities from 2.1 to 4.5 GV, showing that the D flux is more modulated than the ^{4}He flux in this rigidity range. Instead, $k_{^3\mathrm{He}}$ is significantly below zero for rigidities from 1.9 to 3 GV, showing that the ^{3}He flux is less modulated than the ^{4}He flux in this rigidity range, in agreement with our previous measurements in Ref. [12]. k_D is compatible with zero above 4.5 GV and $k_{^3\mathrm{He}}$ is compatible with zero above 3 GV, showing that D flux ratio is time independent above 4.5 GV and ^{3}He/^{4}He flux ratio is time independent above 3 GV.

The time-averaged D, ^{3}He, and ^{4}He fluxes and the corresponding flux ratios are reported in Tables S100 to S102 in the Supplemental Material [20,33] as functions of rigidity, including statistical and systematic errors.

Figure 3(a) shows the time-averaged D and ^{3}He fluxes. As seen, the difference between the two fluxes increases with rigidity. Figure 3(b) shows the time average $D/^3$He flux ratio, which increases with rigidity above ~3 GV. In this and the subsequent figure, the data points are placed along the abscissa at $\tilde{R}$ calculated for a flux $\propto R^{-2.7}$ [38].

The time-averaged flux ratios of D and ^{3}He/^{4}He as functions of rigidity are shown in Fig. 4(a). Above 4.5 GV these ratios are well described by a single power law $C(R/4.5\ \mathrm{GV})^{\Delta}$. For the D/^{4}He flux ratio the fit yields: $\Delta_{\mathrm{D}/^4\mathrm{He}} = -0.108 \pm 0.005$ and $C_{\mathrm{D}/^4\mathrm{He}} = 0.170 \pm 0.003$ with a χ^2/d.o.f. of 10/16. For the ^{3}He/^{4}He flux ratio the fit yields: $\Delta_{^3\mathrm{He}/^4\mathrm{He}} = -0.289 \pm 0.003$ and $C_{^3\mathrm{He}/^4\mathrm{He}} = 0.142 \pm 0.003$ with a χ^2/d.o.f. of 20/16. Unexpectedly, the $D/^4$He flux ratio spectral index is different from that observed for the ^{3}He/^{4}He flux ratio. The significance of $\Delta_{\mathrm{D}/^4\mathrm{He}} > \Delta_{^3\mathrm{He}/^4\mathrm{He}}$ exceeds 10σ. This shows that cosmic deuterons have a sizable primarylike component. The excess of the D flux at high rigidities is also apparent

when comparing the AMS $D/^4$He flux ratio with cosmic ray propagation model predictions [34,35], see Fig. 1.

To study the differences in the rigidity dependence of D and of primary p, the D/p flux ratio was computed and shown in Fig. 4(b) as a function of rigidity. As seen, the D/p flux ratio is increasing with rigidity. To establish the rigidity interval where the D and p fluxes may have an identical rigidity dependence, the D/p flux ratio above 4.5 GV has been fit with

$$D/p = \begin{cases} C(R/R_0)^{\delta}, & R \le R_0, \\ C, & R > R_0. \end{cases} \quad (4)$$

The fit yields $C = 0.027 \pm 0.001$, $\delta = 0.10 \pm 0.01$, and $R_0 = 13 \pm 1$ GV with a χ^2/d.o.f. of 14/15. This shows that the D and p fluxes have a nearly identical rigidity dependence above ~13 GV, further supporting the conclusion that the deuterons have a primarylike component. Figure 4(b) also shows the ^{3}He$/p$ flux ratio together with the power-law fit result with $C(R/13\ \text{GV})^{\Delta}$ above R_0. The fit yields $C = 0.018 \pm 0.001$, $\Delta = -0.13 \pm 0.03$ with a χ^2/d.o.f. of 1.4/4. As seen, the rigidity dependence of the D/p and ^{3}He$/p$ flux ratios are very different.

Finally, we determine the amount of the primary and secondary components of the D flux using our cosmic ray propagation independent method developed in Refs. [39,40]. To obtain primary Φ_D^P and secondary Φ_D^S components in the D flux Φ_D we fit $\Phi_D = \Phi_D^P + \Phi_D^S$ to the weighted sum of a characteristic primary cosmic ray flux, namely, ^{4}He ($\Phi_{^4\text{He}}$), and of a characteristic secondary cosmic ray flux, namely, ^{3}He ($\Phi_{^3\text{He}}$), above 4.5 GV. The fit yields $\Phi_D^P = (0.094 \pm 0.005) \times \Phi_{^4\text{He}}$ and $\Phi_D^S = (0.58 \pm 0.05) \times \Phi_{^3\text{He}}$ with a χ^2/d.o.f. $= 6/16$ as shown in Fig. 5.

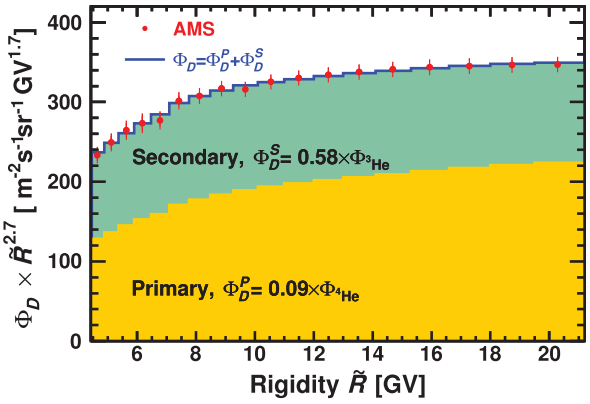

FIG. 5. The AMS time-averaged Φ_D (red circles) multiplied by $\tilde{R}^{2.7}$ as a function of rigidity with total errors above 4.5 GV together with the fit to the weighted sum of $\Phi_{^4\text{He}}$ and $\Phi_{^3\text{He}}$ (blue curve). The contributions of the primary and secondary components are indicated by the yellow and green shadings, respectively. The fit is in excellent agreement with the data.

In conclusion, precision measurements of the cosmic ray D flux have been presented in the rigidity range from 1.9 to 21 GV. We observed that over the entire rigidity range the D flux exhibits nearly identical time variations with the p, ^{3}He, and ^{4}He fluxes. Above 4.5 GV, the $D/^4$He flux ratio is time independent and its rigidity dependence is well described by a single power law $\propto R^{\Delta}$ with $\Delta_{D/^4\text{He}} = -0.108 \pm 0.005$. This is in contrast with the ^{3}He$/^4$He flux ratio for which we find $\Delta_{^3\text{He}/^4\text{He}} = -0.289 \pm 0.003$. The significance of $\Delta_{D/^4\text{He}} > \Delta_{^3\text{He}/^4\text{He}}$ exceeds 10σ. Above ~13 GV the rigidity dependence of the D and p fluxes is nearly identical with a D/p flux ratio of 0.027 ± 0.001. These unexpected observations indicate that cosmic deuterons have a sizable primarylike component. With a method independent of cosmic ray propagation, we obtain the primary component of the D flux equal to $9.4 \pm 0.5\%$ of the ^{4}He flux and the secondary component of the D flux equal to $58 \pm 5\%$ of the ^{3}He flux.

We are grateful for important physics discussions with Igor Moskalenko. We thank former NASA Administrator Daniel S. Goldin for his dedication to the legacy of the ISS as a scientific laboratory and his decision for NASA to fly AMS as a DOE payload. We also acknowledge the continuous support of the NASA leadership, particularly Ken Bowersox and of the JSC and MSFC flight control teams that have allowed AMS to operate optimally on the ISS for over twelve years. We are grateful for the support of Regina Rameika and Glen Crawford of the DOE including resources from the National Energy Research Scientific Computing Center under Contract No. DE-AC02-05CH11231. We gratefully acknowledge the strong support from CERN including Fabiola Gianotti, and the CERN IT department including Bernd Panzer-Steindel. We also acknowledge the continuous support from MIT and its School of Science, Nergis Mavalvala, and the Laboratory for Nuclear Science, Boleslaw Wyslouch. Research supported by Chinese Academy of Sciences, Institute of High Energy Physics, Institute of Electrical Engineering, China Academy of Space Technology, National Natural Science Foundation (NSFC), and Ministry of Science and Technology, National Key R&D Program Grants No. 2022YFA1604802 and No. 2022YFA1604803, NSFC Grant No. 12275158, the China Scholarship Council, the provincial governments of Shandong, Jiangsu, Guangdong, Shandong University, and the Shandong Institute of Advanced Technology, China; the Academy of Finland, Project No. 321882, Finland; CNRS/IN2P3 and CNES, France; DLR under Grant No. 50OO1803 and computing support on the JARA Partition of the RWTH Aachen supercomputer, Germany; INFN and ASI under ASI-INFN Agreement No. 2019-19-HH.0, its amendments, No. 2021-43-HH.0, and ASI-University of Perugia Agreement No. 2019-2-HH.0, and the Italian Ministry of University and Research

(MUR) through the program *"Dipartimenti di Eccellenza 2023-2027"* (Grant SUPER-C), Italy; the Consejo Nacional de Humanidades, Ciencias y Tecnologías (CONAHCYT) under Grant No. CF-2019/2042 and UNAM, Mexico; NWO under Grant No. 680-1-004, Netherlands; FCT under Grant No. CERN/FIS-PAR/0013/2019, Portugal; CIEMAT, IAC, CDTI, MCIN-AEI, and ERDF under Grants No. PID2022-137810NB-C21/C22, No. CEX2019-000920-S, and No. JDC2022-049705-I, Spain; the Fondation Dr. Manfred Steuer, Switzerland; Academia Sinica, the National Science and Technology Council (NSTC), formerly the Ministry of Science and Technology (MOST), under Grants No. 111-2123-M-001-004 and No. 111-2112-M-006-029, High Education Sprout Project by the Ministry of Education at National Cheng Kung University, former Presidents of Academia Sinica Yuan-Tseh Lee and Chi-Huey Wong and former Ministers of NSTC (formerly MOST) Maw-Kuen Wu and Luo-Chuan Lee, Taiwan; the Turkish Energy, Nuclear and Mineral Research Agency (TENMAK) under Grant No. 2020TAEK(CERN) A5.H1.F5-26, Türkiye; and NSF Grant No. 2013228 and ANSWERS proposals No. 2149809, No. 2149810, and No. 2149811, LWS NASA Grant/Cooperative Agreement No. 80NSSC20K1819, and FINESST NASA Grant No. 80NSSC21K1392, USA.Consejo Nacional de Ciencia y Tecnología

[*] Deceased.

[†] Also at IRCCS Azienda Ospedaliero-Universitaria di Bologna, Bologna, Italy.

[1] S. D. Friedman, P. Chayer, E. B. Jenkins, T. M. Tripp, G. M. Williger, G. Hébrard, and P. Sonnentrucker, A high-precision survey of the D/H ratio in the nearby interstellar medium, Astrophys. J. **946**, 34 (2023); R. J. Cooke, M. Pettini, and C. C. Steidel, One percent determination of the primordial deuterium abundance, Astrophys. J. **855**, 102 (2018); A. Coc and E. Vangioni, Primordial nucleosynthesis, Int. J. Mod. Phys. E **26**, 1741002 (2017).

[2] B. Coste, L. Derome, D. Maurin, and A. Putze, Constraining Galactic cosmic-ray parameters with $Z \leq 2$ nuclei, Astron. Astrophys. **539**, A88 (2012).

[3] I. A. Grenier, J. H. Black, and A. W. Strong, The nine lives of cosmic rays in galaxies, Annu. Rev. Astron. Astrophys. **53**, 199 (2015); P. Blasi, The origin of galactic cosmic rays, Astron. Astrophys. Rev. **21**, 70 (2013); A. W. Strong, I. V. Moskalenko, and V. S. Ptuskin, Cosmic-ray propagation and interactions in the galaxy, Annu. Rev. Nucl. Part. Sci. **57**, 285 (2007).

[4] M. Aguilar *et al.*, Observation of new properties of secondary cosmic rays lithium, beryllium, and boron by the Alpha Magnetic Spectrometer on the International Space Station, Phys. Rev. Lett. **120**, 021101 (2018).

[5] Y. Génolini, D. Maurin, I. V. Moskalenko, and M. Unger, Current status and desired precision of the isotopic production cross sections relevant to astrophysics of cosmic rays: Li, Be, B, C, and N, Phys. Rev. C **98**, 034611 (2018).

[6] G. Jóhannesson *et al.*, Bayesian analysis of cosmic ray propagation: Evidence against homogeneous diffusion, Astrophys. J. **824**, 16 (2016).

[7] N. Tomassetti, Propagation of H and He cosmic ray isotopes in the Galaxy: Astrophysical and nuclear uncertainties, Astrophys. Space Sci. **342**, 131 (2012).

[8] A. W. Strong and I. V. Moskalenko, Propagation of cosmic-ray nucleons in the galaxy, Astrophys. J. **509**, 212 (1998).

[9] C. Evoli, D. Gaggero, A. Vittino, G. Di Bernardo, M. Di Mauro, A. Ligorini, P. Ullio, and D. Grasso, Cosmic-ray propagation with DRAGON2: I. Numerical solver and astrophysical ingredients, J. Cosmol. Astropart. Phys. 02 (2017) 015.

[10] D. Maurin, F. Donato, R. Taillet, and P. Salati, Cosmic rays below $Z = 30$ in a diffusion model: New constraints on propagation parameters, Astrophys. J. **555**, 585 (2001).

[11] A. Putze, L. Derome, and D. Maurin, A Markov chain Monte Carlo technique to sample transport and source parameters of Galactic cosmic rays II. Results for the diffusion model combining B/C and radioactive nuclei, Astron. Astrophys. **516**, A66 (2010).

[12] M. Aguilar *et al.*, Properties of cosmic helium isotopes measured by the Alpha Magnetic Spectrometer, Phys. Rev. Lett. **123**, 181102 (2019).

[13] P. Papini *et al.*, High-energy deuteron measurement with the CAPRICE98 experiment, Astrophys. J. **615**, 259 (2004).

[14] M. Aguilar *et al.*, The Alpha Magnetic Spectrometer (AMS) on the International Space Station: Part I—results from the test flight on the space shuttle, Phys. Rep. **366**, 331 (2002); M. Aguilar *et al.*, Isotopic composition of light nuclei in cosmic rays: Results from AMS-01, Astrophys. J. **736**, 105 (2011).

[15] J. Z. Wang *et al.*, Measurement of cosmic-ray hydrogen and helium and their isotopic composition with the BESS experiment, Astrophys. J. **564**, 244 (2002); Z. D. Myers *et al.*, Cosmic ray ^{3}He and ^{4}He spectra from BESS 98, *International Cosmic Ray Conference 2003* (2003), Vol. 4, p. 1805, http://adsabs.harvard.edu/abs/2003ICRC....4.1805M.

[16] G. A. de Nolfo *et al.*, A measurement of cosmic ray deuterium from 0.5–2.9 GeV/nucleon, AIP Conf. Proc. **528**, 425 (2000).

[17] O. Adriani *et al.*, Measurements of cosmic-ray hydrogen and helium isotopes with the PAMELA experiment, Astrophys. J. **818**, 68 (2016).

[18] M. Aguilar *et al.*, The Alpha Magnetic Spectrometer (AMS) on the International Space Station: Part II—Results from the first seven years, Phys. Rep. **894**, 1 (2021).

[19] A. Kounine, The Alpha Magnetic Spectrometer on the International Space Station, Int. J. Mod. Phys. E **21**, 1230005 (2012); S. Ting, The Alpha Magnetic Spectrometer on the International Space Station, Nucl. Phys. B, Proc. Suppl. **243–244**, 12 (2013); B. Bertucci, The AMS-02 detector operation in space, Proc. Sci. EPS-HEP2011 (**2011**) 67; M. Incagli, Astroparticle physics with AMS02, AIP Conf. Proc. **1223**, 43 (2010); R. Battiston, The antimatter spectrometer (AMS-02): A particle physics detector in space, Nucl. Instrum. Methods Phys. Res., Sect. A **588**, 227 (2008).

[20] See Supplemental Material at http://link.aps.org/supplemental/10.1103/PhysRevLett.132.261001 for the AMS detector description, details and figures of the event selection, the background subtraction, the unfolding procedure, and the tabulated time dependence and time average of the D, ^{3}He, ^{4}He fluxes and their ratios.

[21] K. Lübelsmeyer *et al.*, Upgrade of the Alpha Magnetic Spectrometer (AMS-02) for long term operation on the International Space Station (ISS), Nucl. Instrum. Methods Phys. Res., Sect. A **654**, 639 (2011).

[22] B. Alpat *et al.*, The internal alignment and position resolution of the AMS-02 silicon tracker determined with cosmic-ray muons, Nucl. Instrum. Methods Phys. Res., Sect. A **613**, 207 (2010).

[23] G. Ambrosi, V. Choutko, C. Delgado, A. Oliva, Q. Yan, and Y. Li, The spatial resolution of the silicon tracker of the Alpha Magnetic Spectrometer, Nucl. Instrum. Methods Phys. Res., Sect. A **869**, 29 (2017).

[24] Y. Jia, Q. Yan, V. Choutko, H. Liu, and A. Oliva, Nuclei charge measurement by the Alpha Magnetic Spectrometer silicon tracker, Nucl. Instrum. Methods Phys. Res., Sect. A **972**, 164169 (2020).

[25] Q. Yan and V. Choutko, Alignment of the Alpha Magnetic Spectrometer (AMS) in space, Eur. Phys. J. C **83**, 245 (2023).

[26] V. Bindi *et al.*, Calibration and performance of the AMS-02 time of flight detector in space, Nucl. Instrum. Methods Phys. Res., Sect. A **743**, 22 (2014).

[27] M. Aguilar *et al.*, In-beam aerogel light yield characterization for the AMS RICH detector, Nucl. Instrum. Methods Phys. Res., Sect. A **614**, 237 (2010); F. Giovacchini, J. Casaus, and A. Oliva, The AMS-02 RICH detector: Status and physics results, Nucl. Instrum. Methods Phys. Res., Sect. A **952**, 161797 (2020).

[28] J. Allison *et al.*, Recent developments in GEANT4, Nucl. Instrum. Methods Phys. Res., Sect. A **835**, 186 (2016); J. Allison *et al.*, GEANT4 developments and applications, IEEE Trans. Nucl. Sci. **53**, 270 (2006); S. Agostinelli *et al.*, GEANT4 a simulation toolkit, Nucl. Instrum. Methods Phys. Res., Sect. A **506**, 250 (2003).

[29] J. Alcaraz *et al.*, Leptons in near earth orbit, Phys. Lett. B **484**, 10 (2000).

[30] C. C. Finlay *et al.*, International geomagnetic reference field: The eleventh generation, Geophys. J. Int. **183**, 1216 (2010); E. Thébault *et al.*, International geomagnetic reference field: The 12th generation, Earth Planets Space **67**, 79 (2015); Geomagnetic Field Modeling Working Group, IGRF-13 model, 2019, https://www.ngdc.noaa.gov/IAGA/vmod/igrf.html.

[31] G. H. Gene, P. C. Hansen, and D. P. O'Leary, Tikhonov regularization and total least squares, SIAM J. Matrix Anal. Appl. **21**, 185 (1999); P. C. Hansen and D. P. O'Leary, The use of the L-curve in the regularization of discrete Ill-posed problems, SIAM J. Sci. Comput. **14**, 1487 (1993).

[32] M. Aguilar *et al.*, Precision measurement of the proton flux in primary cosmic rays from rigidity 1 GV to 1.8 TV with the Alpha Magnetic Spectrometer on the International Space Station, Phys. Rev. Lett. **114**, 171103 (2015).

[33] Note that the data can also be downloaded in different formats from the AMS website https://ams02.space/sites/default/files/publication/202401/table-s1-s99.csv; https://ams02.space/sites/default/files/publication/202401/table-s100.csv; https://ams02.space/sites/default/files/publication/202401/table-s101.csv; and https://ams02.space/sites/default/files/publication/202401/table-s102.csv; the ASI cosmic-ray database at https://tools.ssdc.asi.it/CosmicRays; and the LPSC cosmic-ray database at https://lpsc.in2p3.fr/crdb/.

[34] D. M. Gomez-Coral, C. Gerrity, R. Munini, and P. von Doetinchem, Current status and new perspectives on cosmic ray deuterons, Phys. Rev. D **107**, 123008 (2023).

[35] N. Weinrich, Y. Génolini, M. Boudaud, L. Derome, and D. Maurin, Combined analysis of AMS-02 $(\mathrm{Li}, \mathrm{Be}, \mathrm{B})/\mathrm{C}$, N/O, ^{3}He, and ^{4}He data, Astron. Astrophys. **639**, A131 (2020). We are grateful to D. Maurin for providing the cosmic ray propagation model USINE predictions for the $\mathrm{D}/^4\mathrm{He}$ and D/He flux ratios as functions of kinetic energy per nucleon, which enable us to compare the model with our current data.

[36] D. Maurin, F. Melot, and R. Taillet, A database of charged cosmic rays, Astron. Astrophys. **569**, A32 (2014).

[37] M. Aguilar *et al.*, Periodicities in the daily proton fluxes from 2011 to 2019 measured by the Alpha Magnetic Spectrometer on the International Space Station from 1 to 100 GV, Phys. Rev. Lett. **127**, 271102 (2021). The new Φ_p data up to April 2021 will be published separately.

[38] G. D. Lafferty and T. R. Wyatt, Where to stick your data points: The treatment of measurements within wide bins, Nucl. Instrum. Methods Phys. Res., Sect. A **355**, 541 (1995). We have used Eq. (6) with $\tilde{R} \equiv x_{lw}$.

[39] M. Aguilar *et al.*, Properties of a new group of cosmic nuclei: Results from the Alpha Magnetic Spectrometer on sodium, aluminum, and nitrogen, Phys. Rev. Lett. **127**, 021101 (2021).

[40] M. Aguilar *et al.*, Properties of cosmic-ray sulfur and determination of the composition of primary cosmic-ray carbon, neon, magnesium, and sulfur: Ten-year results from the Alpha Magnetic Spectrometer, Phys. Rev. Lett. **130**, 211002 (2023).